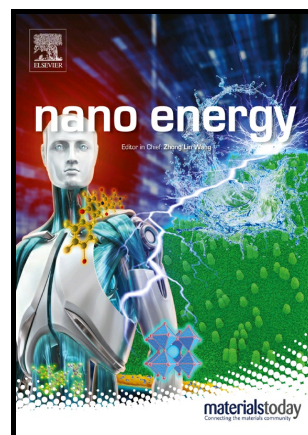# Journal Pre-proof

Enhanced Solar Photoreduction of CO_2 to Liquid Fuel over rGO Grafted NiO-CeO$_2$ Heterostructure Nanocomposite

Hong Ryeol Park, Amol Uttam Pawar, Umapada Pal, Tierui Zhang, Young Soo Kang

This is a PDF file of an article that has undergone enhancements after acceptance, such as the addition of a cover page and metadata, and formatting for readability, but it is not yet the definitive version of record. This version will undergo additional copyediting, typesetting and review before it is published in its final form, but we are providing this version to give early visibility of the article. Please note that, during the production process, errors may be discovered which could affect the content, and all legal disclaimers that apply to the journal pertain.

Enhanced Solar Photoreduction of CO_2 to Liquid Fuel over rGO Grafted NiO-CeO$_2$ Heterostructure Nanocomposite

Hong Ryeol Park[§⊥], Amol Uttam Pawar[§⊥], Umapada Pal[§#], Tierui Zhang[$] and Young Soo Kang*[§]

[§]Department of Chemistry, Sogang University, #1 Shinsu-dong, Mapo-gu, Seoul 121-742, Republic of Korea
[$]Key Laboratory of Photochemical Conversion and Optoelectronics Materials, Technical Institute of Physics and Chemistry (TIPC), Chinese Academy of Sciences (CAS), Beijing 100190, China
[#] On leave from Institute of Physics, Autonomous University of Puebla, Mexico.

[⊥] H. R. Park and A. U. Pawar contributed equally.

* Corresponding author e-mail: yskang@sogang.ac.kr

Abstract

Intrinsic oxygen vacancies at CeO_2 surface are known to activate thermodynamically stable CO_2 molecules, enhancing the reaction rate and reducing reduction energy. However, charge recombination at the ceria-based cathode surface suppresses the multi-electron transfer process required for a complete reduction of CO_2 molecules to generate useful hydrocarbons. To suppress this charge recombination and facilitate the multi-electron transfer process, p-type NiO and reduced graphene oxide (rGO) were hybridized with CeO_2 to form rGO-grafted NiO-CeO_2 photocatalyst, which can convert CO_2 to formaldehyde at a rate of 421.09 μmol g^{-1} h^{-1}; about 4 times higher than that of pristine CeO_2. Formation of photo-induced oxygen vacancy of CeO_2 photocatalyst resulted in a change of Ce-O bond length at ceria surface were monitored *in-situ* by X-ray absorption near edge structure (XANES), and X-ray absorption fine structure (EXAFS) spectroscopy. Tracking the formation of CO_2 anion radical ($CO_2^{•-}$) and its subsequent protonation

with *in-situ* electron paramagnetic resonance spectroscopy and attenuated total reflection-infrared (ATR-IR) spectroscopy, mechanism and reaction pathway of CO_2 reduction into formaldehyde formation have been elucidated.

Graphical Abstract

Schematic representation of rGO grafted $NiO-CeO_2$ nanocomposite and Photocatalytic CO_2 reduction process with experimental CO_2 reduction yield.
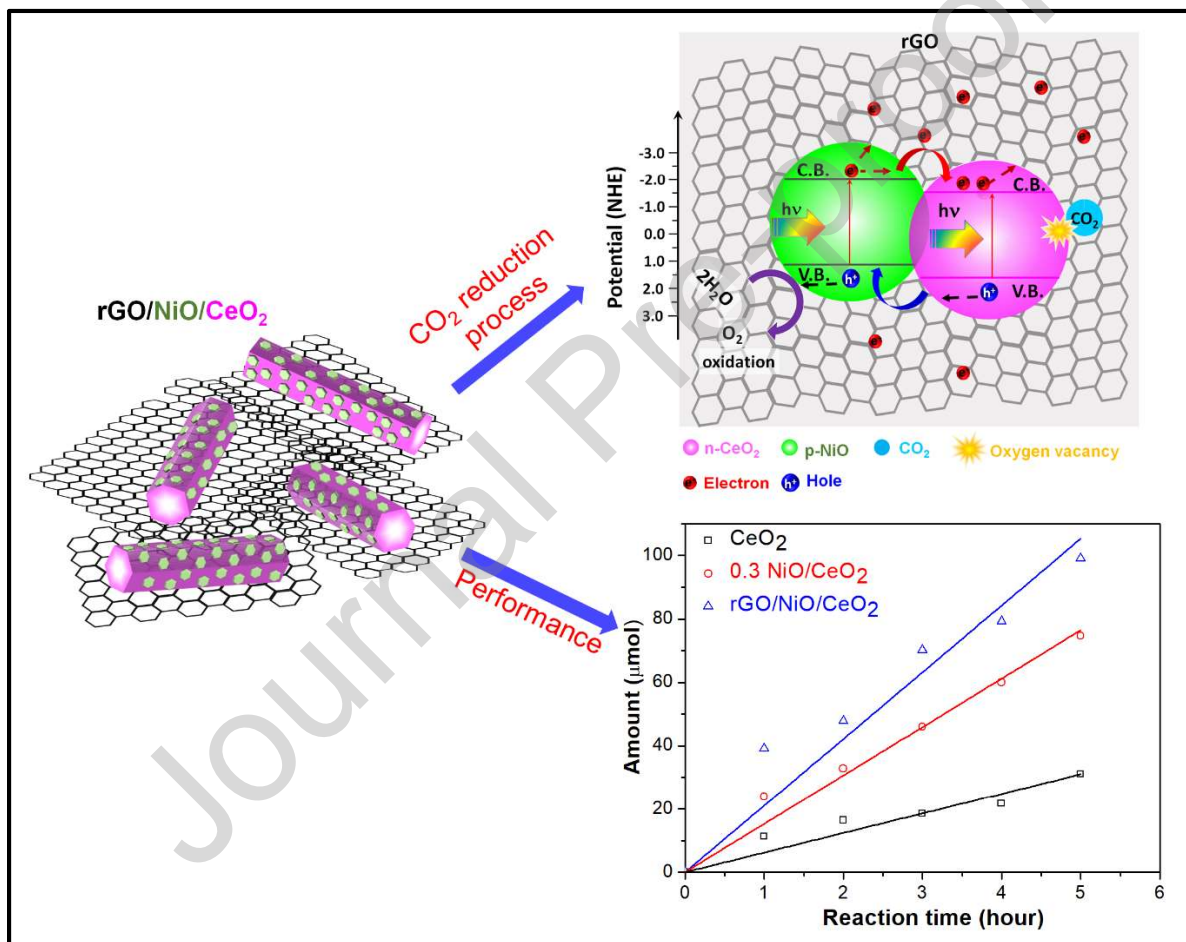
Keywords: Photocatalytic CO_2 reduction • Oxygen vacancy • CO_2 activation • CO_2 reduction mechanism • *In-situ* XAFS/ATR-IR

Introduction

Anthropogenic CO_2 emission led by excessive fossil fuel usage has increased its concentration in the earth's atmosphere to unprecedented level.[1] Therefore, finding ways to prevent the climatic change driven by CO_2 surge is one of the most urgent tasks for the scientific community. While a variety of solutions such as capturing CO_2 in rocks,[2] making CO_2-based copolymers such as polypropylene carbonate (PPC),[3] and electrochemical CO_2 reduction [4-7] have been suggested for the capture and utilization of CO_2, all these methods require external energy to activate, reduce, and convert CO_2 into fuel products due to its high thermodynamic stability. As the search for cost-effective efficient methods for CO_2 reduction is continued, utilization of cheap renewable energy might be a viable alternative for producing high energy chemicals through CO_2 photoreduction in cheaper way. Solar light is one of the sustainable, abundant, and cheaper energy sources, which has been utilized for the reduction of CO_2 and its conversion to fuel. Photoelectrochemical (PEC) and photocatalytic (PC) CO_2 reductions have been carried out using solar light. Taking the advantage of solar light as cheap energy source, PEC and PC CO_2 reductions have been performed over several semiconductor photocatalysts. Use of different semiconductor photocatalysts yielded different solar fuels such as methanol, ethanol and formaldehyde.[8-10] During the past two decades, various semiconductors such as TiO_2, CdS, $CaFe_2O_4$, ZnO, and TaON have been tested as photocatalysts for CO_2 reduction.[11-15] However, low efficiency and poor product selectivity of CO_2 reduction remained the principal obstacles for practical application of these photocatalysts.

Recently, several research groups have tested cerium (IV) dioxide (CeO_2) as photocatalyst for CO_2 reduction, which is an n-type semiconductor, commonly used as solid oxide fuel cell catalyst and photocatalyst. It also has quite good ability for adsorbing and activating CO_2

3

molecule which bears high activation energy. Activation of CO_2 molecule by adsorption at the ceria surface occurs though deformation of its linear molecular structure, which also accelerates its reduction rate due to decreased activation energy. However, this barely occurs without association of specific activators such as *N*-heterocyclic compounds and amines.[16] Owing to the facile reducing and oxidizing properties of Ce^{4+}/Ce^{3+} ions, a large number of oxygen vacancies are formed at CeO_2 surface under solar light illumination, which activate CO_2 molecules.[17] According to the previous reports based on density functional theory (DFT) calculation and spectroscopic studies, oxygen vacancies in CeO_2 particles can effectively activate a CO_2 molecule adsorbed at their surface by deforming its linear O=C=O bond structure,[18-20] which can be reduced easily with low activation energy and less reduction reaction energy as presented in **Figure 1a**.

Even though the CO_2 molecules can be activated over CeO_2 surface, utilization of CeO_2 alone does not guaranty a high efficiency of their photocatalytic reduction, as the diffusion length of charge carriers in CeO_2 is short, which results in a fast recombination of photo-generated charge carriers. As a solution of this problem, CeO_2 nanoparticles or thin films have been hybridized with *p*-type semiconductor photocatalysts to suppress charge carrier recombination and enhance the charge collection efficiency of the photocatalyst surface. Till date, several semiconductors and metals have been tested as possible counterparts of CeO_2 for the formation of interface junction, to enhance its photocatalytic activity by suppressing charge recombination.[20-27] However, no significant enhancement in its CO_2 reduction activity achieved so far.

In this study, we combined p-type NiO particles with n-type CeO_2 particles to form p-n junction interfaces, which can suppress the charge carrier recombination process at the surface of CeO_2 nanoparticles.[23,28] As the conduction band (CB) and valence band (VB) energy levels of NiO

remain at higher and lower energy positions to those of CeO_2 (**Figure 1b**), respectively, the photogenerated electrons and holes at $NiO-CeO_2$ interface diffuse spontaneously in opposite directions, reducing the probability of their recombination. Further, we introduced reduced graphene oxide (rGO) in the composite to exploit its high electrical conductivity and charge trapping behavior, which allowed an easy accumulation of electrons at the hybrid composite photocatalyst surface and subsequent sequential multi-electron transfer at each of the intermediate steps of CO_2 reduction process. The sequential multi-electron transfer process induces photocatalytic reduction of CO_2 molecules adsorbed and activated at CeO_2 surface, producing formaldehyde as liquid fuel at 421.09 μmol g^{-1} h^{-1} rate.

Result and Discussion

The $NiO/CeO_2/rGO$ hybrid composite photocatalyst was prepared by hydrothermal process (see Supporting Information). The hybrid composite includes CeO_2 nanorods with {100} crystal facets interfaced with NiO nanoparticles. Furthermore, the nanorods were covered with rGO layers (see **Figure 2**). The photocatalyst revealed an enhanced CO_2 reduction performance for generating formaldehyde selectively, along with the emission of hydrogen gas in nominal quantity. Through time-resolved photoluminescence (TRPL) spectroscopy and *in-situ* gas chromatography (GC), we could confirm that the enhanced CO_2 reduction ability of the $NiO/CeO_2/rGO$ hybrid composite photocatalyst is associated to the reduced charge recombination at $NiO-CeO_2$ interface and enhanced sequential multi-electron transfer (from the photocatalyst to activated CO_2 molecules) ability of rGO. The CO_2 molecules adsorbed at the CeO_2 surface of the $NiO/CeO_2/rGO$ hybrid composite photocatalyst are activated to monodentate CO_2 and reduced to formaldehyde via formate intermediate.

Crystallinity and structural behavior of the fabricated CeO_2, NiO/CeO_2 and $NiO/CeO_2/rGO$ nanostructures were studied by powder X-ray diffraction (XRD) (**Figure S1**, Supporting Information) spectroscopy. As can be seen in **Figure S1**, major diffraction peaks appeared in the XRD pattern of the CeO_2 catalyst correspond to fluorite-type CeO_2 (PDF#43-1002) lattice. On the other hand, XRD patterns of the NiO/CeO_2 nanostructures and $NiO/CeO_2/rGO$ hybrid composite photocatalyst revealed weaker diffraction bands of NiO, along with intense diffraction bands associated to CeO_2. Intensity of the diffraction bands correspond to NiO did not vary significantly with the variation of NiO content in the hybrid composite catalyst. Finally, the XRD pattern of the $NiO/CeO_2/rGO$ hybrid photocatalyst (prepared with 30 mol% NiO) revealed similar features as that of the 0.3 NiO/CeO_2 nanostructures, which is in good agreement with the amorphous nature of rGO and its lower content in the hybrid composite. Although a prolonged photocatalytic reaction (in **Figure S1**, Supporting Information) reduces the crystallinity of the hybrid composite, its crystallinity could be recovered by air-annealing at 350 ^{o}C for 4 h (see Supporting Information). For a detailed microstructural investigation of the CeO_2, 0.3 NiO/CeO_2, and $NiO/CeO_2/rGO$ nanostructures, their high resolution TEM (HRTEM) images (**Figure 2**) were recorded. As can be seen, fabricated CeO_2 nanorods have exposed facets of {100} crystal planes. Unlike the pristine CeO_2 nanorods, the surface of CeO_2 nanorods in NiO/CeO_2 nanostructures appear blunt, due to the coverage by NiO nanodisks. On adding Ni^{2+} ion precursor in the alkaline reaction mixture, $Ni(OH)_2$ seeds were generated, which adhered with the CeO_2 seeds.[29] During hydrothermal treatment and subsequent Ar annealing, the $Ni(OH)_2$ particles transformed to NiO particles attaching with CeO_2 nanorods. As can be seen in the HRTEM image provided as inset of **Figure 2a**, the lattice fringes are arranged parallel to the crystal facet of the CeO_2 nanorods, with average d-spacing of 2.75 Å, which corresponds to the

{100} lattice planes of fluorite-type CeO_2. In the case of NiO/CeO_2 nanostructures (**Figure 2b**), thin hexagon-shaped crystalline NiO plates remained attached to the CeO_2 nanorods. Average interplanar spacing (2.46 Å) estimated from the lattice fringes corresponds well to the (111) lattice planes of NiO. No significant change could be observed in the microstructure of the hybrid composite photocatalyst even after its prolonged (15 h) utilization in photocatalytic reaction. The steps involved in the formation of $NiO/CeO_2/rGO$ hybrid composite have been schematically illustrated in **Figure 2**.

Energy dispersive X-ray (EDX) analysis was carried out inside a transmission electron microscope to check the atomic ratio of elements and their distribution in the samples (**Figures S2** and **S3**, Supporting Information). While the NiO/CeO_2 nanostructures revealed only Ni, Ce and O atoms in them, the $NiO/CeO_2/rGO$ hybrid composite revealed Ni, Ce, O and C as its constituents, indicating rGO coverage of the NiO/CeO_2 nanostructures. The results of quantitative elemental analysis (**Figure S3**, Supporting Information) of the fabricated nanostructures are consistent with the nominal concentration of each of the elements (precursors) in corresponding reaction mixtures.

Optical band gap energy values of the NiO, CeO_2, 0.3 NiO/CeO_2, and $NiO/CeO_2/rGO$ nanostructures were estimated from the Kubelka-Munk plots of their UV-Vis absorption spectra (**Figure S4**, Supporting Information) recorded in diffuse reflection mode. As can be noticed, absorption efficiency of the CeO_2 nanostructures increases due to incorporation of NiO nanoparticles (**Figure S4a**, Supporting Information). Observed higher absorbance of the NiO/CeO_2 sample can be associated to the blackish color of the NiO particles, which probably contain a fraction of unoxidized Ni atoms (i.e. Ni^0) due to incomplete oxidation during annealing (at 350 ^{o}C, 4 h). However, the presence of Ni^0 species in the sample might be a blessing in

7

disguise for its photocatalytic application, as the light absorption ability of Ni^0 species containing NiO particles has been seen to be significantly higher than that of fully oxidized NiO particles.[30] As can be noticed in **Figure S4** (Supporting Information), the band gap energy estimated for the NiO sample prepared using the same method used for the preparation of NiO/CeO$_2$ nanostructures is about 3.42 eV, which is lower than the band gap energy of stoichiometric NiO (4.30 eV). [31] Due to the same reason, the interface potential barrier in the heterojunction nanostructures is small (**Fig. 4a**). While a higher interface potential would help to reduce the recombination rate of the photogenerated charge carriers at the NiO-CeO$_2$ interface, presence of metallic Ni helps to absorb more photons, generating higher number of electron-hole pairs. Absorption coefficient of the NiO/CeO$_2$ nanostructures increased further due to rGO grafting (**Figure S4**, Supporting Information). Band gap energy of the hybrid composite photocatalyst suffered a red-shift both due to the incorporation of NiO and rGO, effectively shifting it towards visible spectral region. Observed reduction of band gap energy can be associated both to the coupling of CeO$_2$ with NiO particles to form p-n junction at their interface and incorporation of rGO in the heterojunction nanostructures. As can be seen in **Figure S4a** (Supporting Information), rGO alone, prepared by similar hydrothermal reduction of GO has a strong absorbance in the UV-Vis (400 to 700 nm) spectral range, which causes a net shift of absorption spectrum of the hybrid composite photocatalyst (NiO/CeO$_2$/rGO) towards higher wavelength. Estimated band gap energy (E_g) values for CeO$_2$, NiO, NiO/CeO$_2$, and 0.3 NiO/CeO$_2$/rGO nanostructures were determined as 3.30, 3.42, 3.07, and 2.81 eV, respectively.

To estimate the valence band (VB) position of the photocatalysts, they were analyzed by ultraviolet photoelectron spectroscopy (UPS) (**Figure S5,** Supporting Information). Valence band maximum energy (E_{VBM}) values of the pristine CeO$_2$ and NiO were determined to be of

3.88 and 1.09 eV, respectively. Estimated secondary cut-off energies (E_{SCE}) of the nanostructures were 19.09 and 16.47 eV, respectively. The valence band position with respect to NHE energy level (E_{NHE}) could be calculated using equation (1):

$$\mathbf{E_{NHE}} = -21.21 - (E_{VBM} - E_{SCE}) + 4.50 \qquad (eV \ vs. \ NHE) \qquad (1)$$

Estimated VB energies of CeO_2 and NiO were 1.50 and 1.33 eV (vs. NHE), respectively. Conduction band potentials of the photocatalysts were calculated from their optical band gap energy and valence band energy values. Conduction band energies of CeO_2 and NiO were determined to be of -1.80 and -2.09 eV (vs. NHE), respectively. A tentative energy band diagram for the NiO/CeO_2 hybrid photocatalyst has been presented in **Figure 3a**. The cascade flow of electrons from the conduction band of NiO to rGO in the band-aligned heterostructure can be easily followed in the scheme illustrated in **Figure 1**. On solar light illumination, the holes generated in the VB of CeO_2 move to the VB of NiO spontaneously. As the difference between the conduction band position of CeO_2 and valence band maximum of NiO_2 is higher than the reduction and oxidation potential of CO_2 and H_2O, respectively, the photo-generated electrons and holes have enough energy to execute simultaneous oxidation and reduction reactions at the surface of the catalyst under solar light illumination. On the other hand, electrons are accumulated at the surface of rGO have sufficient energy to reduce CO_2 into formaldehyde (reduction potential = -0.48 V vs NHE).

XPS analysis results of the $NiO/CeO_2/rGO$ photocatalyst are presented in **Figure S6** (Supporting Information). As can be seen in **Figure S6a**, cerium remained both in its Ce^{4+} and Ce^{3+} oxidation states in the sample. On the other hand, while nickel in the NiO particles remained predominantly in Ni^{2+} state, a minor amount fraction remained in Ni^0 state, producing a component band around 852.7 eV in the Ni 2p core-level region (**Figure S6b,** Supporting

Information). Metallic nickel (Ni^0) fractions in the photocatalyst estimated from peak area ratio of the Ni 2p components were about 43.0 and 40.3 % before and after 15 h of CO_2 reduction reaction (**Figure S7b** and **Table S1**, Supporting Information), respectively.

The C 1s core-level emission presented in **Figure S6c** (Supporting Information) shows the degree of reduction of rGO covering the NiO/CeO_2 nanostructures. Higher intensities of the C=C and C-C components compared to other oxygen bound carbon peaks indicate adequate reduction of GO. The O 1s core-level emission presented in **Figure S6d** (Supporting Information) clearly revealed two components. The predominant component appeared at 528.4 eV corresponds to Ce^{4+} bound oxygen atoms, and the weaker component at 531.2 eV corresponds to Ce^{3+} bound oxygen atoms. Appearance of Ce^{3+} bound oxygen signal in the sample clearly indicates the presence of oxygen vacancies at CeO_2 surface. In addition, there appeared emission peaks around 529.1, 530.3, 532.2, and 533.2 eV. While the emission peak revealed at 529.1 eV could be associated to Ni^{2+} bound oxygen atoms originated from NiO, the peaks appeared at 530.3 eV, 532.2 eV and 533.2 eV correspond to O-C=O, C=O, and C-O, respectively, all originating from rGO.

As can be seen in the EIS Nyquist plots (**Figure S8a**, Supporting Information), the impedance of the photocatalysts decreases in the order CeO_2 > NiO/CeO_2 > $NiO/CeO_2/rGO$, indicating an increase in charge collection efficiency due to rGO grafting. To verify the formation of p-n junction at $NiO-CeO_2$ interface, Mott–Schottky plots were drawn for the CeO_2 and 0.3 NiO/CeO_2 nanostructures (**Figure S8b**, Supporting Information), and their slopes were compared. The Mott-Schottky plot of the CeO_2 nanoparticles revealed the characteristic of *n*-type semiconductor, increasing current with bias potential. On the other hand, in the Mott-Schottky plot of the 0.3 NiO/CeO_2 sample, the current increased until -0.1 V (vs. Ag/AgCl) bias

potential and then decreased. The plot resembles to the typical Mott–Schottky plot of a p-n junction, clearly demonstrating the formation of p-n junction at NiO-CeO$_2$ interface.

Typical time-resolved photoluminescence (TRPL) decay curves of the CeO$_2$, 0.3 NiO/CeO$_2$, and NiO/CeO$_2$/rGO nanostructures are presented in **Figure 3b**. The experimentally obtained curves could be fitted to double-exponential equation:

$$I(t) = A_1\, e^{-(\frac{t}{\tau_1})} + A_2 e^{-(\frac{t}{\tau_2})} \qquad (2)$$

where **t** is the elapsed time after pulsed laser excitation, $I(t)$ is the emission intensity at given time **t**, A_1 and A_2 are pre-exponential factors, τ_1 is the fast decay lifetime, and τ_2 is the slow decay lifetime. Average lifetimes of the charge carriers τ_{ave} in the photocatalysts were calculated using the relation (equation 3):[32]

$$\tau_{ave} = (A_1\tau_1^2 + A_2\tau_2^2)/(A_1\tau_1 + A_2\tau_2) \qquad (3).$$

The fitting parameters of the TRPL decay curves are summarized in **Table 1**. As can be noticed, the τ_{ave} value of CeO$_2$ increased from 5.57 to 5.80 ns due to coupling with NiO (i.e. formation of NiO-CeO$_2$ junctions). Such an increase of carrier lifetime in the composite demonstrates a better charge separation at the NiO-CeO$_2$ interface due to the development of space charge induced electric field at p-n junction interface. The electric field produced at the junction interface helps the electrons to migrate from one material to other of different conduction band energy values. As the consequence of such effect, charge carrier recombination at the composite photocatalyst interface get suppressed, enhancing the photocatalytic activity of CeO$_2$ for CO$_2$ reduction.[33,34] On covering the 0.3 NiO/CeO$_2$ nanostructures by rGO sheets (i.e. in NiO/CeO$_2$/rGO hybrid composite nanostructures), a significant decrease in carrier lifetime, along

11

with a reduction in fluorescence intensity was observed. Based on calculated kinetic parameters, the estimated τ_{ave} value for the photocatalyst was 2.16 ns. This remarkable decrease in lifetime of the excited electrons is possibly caused by the attachment rGO sheets at the surface of NiO-CeO_2 nanostructures. rGO is a well-known electron scavenger with high charge holding capacity. Due to the extraction of excited electrons from CeO_2, both the PL intensity and the effective carrier-lifetime in the NiO/CeO_2/rGO hybrid catalyst decreased significantly.[35-38] Moreover, due to electron accumulation at its surface, rGO acts as a sequential multi-electron transfer agent for CO_2 reduction to form liquid hydrocarbon fuels.[39] The electrons accumulated in rGO sheet could be transferred to the activated CO_2 molecules at the surface of CeO_2 to initiate its reduction reaction. The flow direction of photo-excited electrons in the NiO/CeO_2/rGO hybrid composite structure is determined by the conduction band alignment in it, as shown in the scheme depicted in **Figure 3a**.

Although the photoreduction of Ce^{4+} to Ce^{3+} in stoichiometric CeO_2 has been probed by Fujishiro's group [40] using PL spectra analysis,[40] they did not provide any direct evidence of oxygen vacancy formation at CeO_2 surface due to solar light irradiation. Thus, we carried out *in-situ* XANES analysis of the NiO/CeO_2/rGO hybrid composite photocatalyst under simulated solar light illumination in the "light on-off" conditions to identify the change in surface atomic structure of the NiO/CeO_2/rGO hybrid composite photocatalyst due to solar light illumination. From the *in-situ* XANES analysis results presented in **Figure 4a**, it can be seen that under dark (i.e. in absence of illuminating light) the XANES spectrum of the NiO/CeO_2/rGO hybrid composite photocatalyst is dominated by two absorption bands located at 5730 and 5737 eV, which correspond to the typical near-edge absorption bands of Ce^{4+}. The minor shoulder peak appeared around 5726 eV corresponds to the near-edge absorption band of Ce^{3+} ions. These

results clearly demonstrate that most of the Ce atoms in the sample are in Ce^{4+} oxidation state. Trace amount of Ce^{3+} detected in the pristine (not presented) CeO_2 particles probably originated from the unreacted $Ce(NO_3)_3 \cdot 6H_2O$ precursor utilized for their synthesis. On irradiating the photocatalyst by 1 sun solar light, relative intensity of the doublet band with respect to the shoulder band decreased. The enhanced relative intensity of the shoulder band due to solar light illumination is clear in the band-deconvoluted spectra of the sample presented in **Figures 4b** and **4c**. The results clearly demonstrate the ability of solar light for reducing Ce^{4+} to Ce^{3+} at the surface of CeO_2.

To determine the change in atomic bond order at the surface of $NiO/CeO_2/rGO$ hybrid composite photocatalyst during photocatalytic CO_2 reduction process, *in-situ* EXAFS analysis of bond structure around Ce atoms was carried out under three different conditions: (1) light off, without CO_2, (2) light on, without CO_2, and (3) light on, with CO_2 purging. Corresponding plots of Fourier transformed Ce-L3 edge EXAFS spectra for $NiO/CeO_2/rGO$ are presented in **Figure 4d**. The results obtained for condition (1) revealed shortest bond distance of 2.36 Å between the target Ce atom and neighboring O atoms. The value is slightly larger than the EXAFS estimated reported value (2.34 Å) for stoichiometric CeO_2.[41] The observed elongation of the Ce-O bond might be due to the presence of Ce^{3+} in traces at the surface of CeO_2 particles fabricated in this work. Under condition (2), i.e. when the $NiO/CeO_2/rGO$ hybrid photocatalyst was irradiated with solar light without CO_2 purging, the bond distance between Ce atom and adjacent O atoms increased to 2.42 Å. As has been discussed earlier, solar light irradiation can reduce Ce^{4+} ions of CeO_2 surface to Ce^{3+} ions, forming oxygen vacancies. Due to the generation of oxygen vacancies, CeO_2 surface suffers a structural distortion induced by the difference in the ionic radii of Ce^{3+} and Ce^{4+}. As the ionic radius of Ce^{4+} is 1.00 Å, and that of Ce^{3+} is 1.14 Å,[42] the

13

observed 0.08 Å increase in Ce-O bond length is pretty close to its expected 0.07 Å value. In fact, an increase in Ce-O bond length due to reduction of Ce^{4+} ions to Ce^{3+} at the surface of CeO_2 has been detected earlier by EXAFS study.[43]

Based on DFT calculations, McKenzie et al.[44] have reported the occurrence of electron accumulation at oxygen vacancy sites, which causes the reduction of Ce^{4+} to Ce^{3+} over CeO_2 surface. To stabilize the structural strain induced by oxygen vacancies, crystal structural rearrangement occurs at the surface of CeO_2.[44] Structural changes occur at the surface of CeO_2 have been schematically presented in **Figure 3c**. On the formation of oxygen vacancy by expelling the atom O_v, the O1 atom moves slightly closer to Ce1 and Ce2 atoms, and away from the Ce3 atom. As a result, the length of the Ce1(and Ce2)-O1 bond increases. Even though a theoretical calculation, particularly for the ceria {110} surface, has not been reported in the literature, our EXAFS fitting results clearly revealed an increase in the Ce-O bond length on the formation of oxygen vacancies at ceria surface. While these oxygen vacancies act as CO_2 capturing sites at the surface of nonstoichiometric ceria particles, the captured CO_2 molecule acquires a bent structure (**Figure 3c**, column 3) and gets activated to a higher energy state than its stable linear form.[45] On the other hand, excess electrons accumulated in the rGO layer are sequentially transferred to the adsorbed CO_2 molecule, changing it to CO_2 anion radical ($CO_2^{\bullet-}$). In this process, the distance between the Ce and O atom (Ce1-O or Ce2-O) also increases.[18] This might be the reason for largest empirical average Ce-O distance (2.45 Å) we obtained for the hybrid catalyst under condition (3), i.e. in presence of solar light and under CO_2 bubbling, through *in-situ* EXAFS analysis. As can be noticed, this average Ce-O distance value (2.45 Å) is about 0.03 Å larger than that estimated under condition (2), i.e. under solar light illumination, without CO_2 bubbling.

To monitor the CO_2 reduction reaction process on CeO_2 surface and its intermediate steps, radicals produced during CO_2 photoreduction were monitored by trapping them in 5-5-Dimethyl-1-pyrroline N-oxide (DMPO). The captured intermediate radicals were monitored by electron paramagnetic resonance (EPR) spectroscopy at low temperature. As can be noticed in **Figure 5a,** the EPR spectrum recorded on the sample collected before light irradiation is featureless, indicating the presence of trapped $OH^\bullet$ radicals below the detection limit of the EPR system. However, the sample collected after 30 min of photoreduction reaction revealed splitted EPR spectrum (**Figure 5b**) including four peaks, with g value 2.0052 and coupling constant around 22 G, clearly indicating the formation of intermediate $CO_2^{\bullet-}$ anion radicals during photoreduction of CO_2. The EPR spectrum of the sample collected before light illumination to the reaction mixture contained $DMPO:OH^\bullet$, which revealed four peaks due to the interaction of unpaired electrons with nitrogen and hydrogen. Due to singular nuclear spin (i.e. $I = 1$) of nitrogen, it should reveal a triplet under the external magnetic field applied during EPR measurement. As shown in **Figure S11a** (Supporting Information), each of these components splits further into a doublet due to nearby hydrogen ($I = 1/2$). However, as nitrogen and hydrogen nucleii have similar hyperfine splitting constants ($\alpha_N = \alpha_H = 14.9$ G), and produce mixed combined EPR signals,[46,47] the two central peaks overlap, manifesting only four peaks of intensity ratio 1:2:2:1. When $CO_2^{\bullet-}$ anion radicals are capture by DMPO, the hyperfine splitting constants of nitrogen and hydrogen change to $\alpha_N = 15.6$ G and $\alpha_H = 19$ G,[47] producing six clear peaks in the spectrum as demonstrated in **Figure S11b** (Supporting Information). However, presence of both $DMPO:CO_2^{\bullet-}$ and $DMPO:OH^\bullet$ radicals in the sample can cause peak broadening, resulting in only four peaks in the EPR signal of the sample collected from the reaction mixture after prolonged photocatalytic reaction. In fact, such a peak broadening and reduction of splitted peaks

in the sample have been associated to the limited mobility of $CO_2^{\bullet-}$ radicals in the solvent, while they have maximum mobility at the surface of the catalyst.[48,49] The obtained results clearly indicate the generation of $CO_2^{\bullet-}$ radicals during the photocatalytic reduction of CO_2 at CeO_2 surface.

To compare the efficiency of CO_2 reduction of the photocatalysts, CO_2 reduction reactions were carried out in a home-made glass reactor. Sodium sulfite was used as a hole scavenger to prevent the degradation of the reduction product by holes and reduce water oxidation rate at the surface of the photocatalyst. Quantitative analysis of the products was performed in an Agilent gas chromatograph (GC) attached with a Teledyne Tekmar Stratum Purge & Trap system for analyzing liquid samples. The GC analysis of the liquid CO_2 reduction reaction products revealed predominant formaldehyde signal, with minor signals of hydrogen and oxygen (**Figure S12**, Supporting Information). The quantity of formaldehyde produced at different irradiation times for the CeO_2, 3.0 NiO/CeO_2, and $NiO/CeO_2/rGO$ photocatalysts are presented in **Figure 5c**. As can be seen, CO_2 reduction efficiency of CeO_2 is the worst among these three photocatalysts. The rate of formaldehyde production by CeO_2 was only 124.09 μmol g^{-1} h^{-1}. Compared to the bare (pristine) CeO_2, the 0.3 NiO/CeO_2 and $NiO/CeO_2/rGO$ photocatalysts produced formaldehyde at much higher rates; 305.98 and 421.09 μmol g^{-1} h^{-1}, respectively. On the other hand, the rate of CO_2 photoreduction by NiO/rGO and CeO_2/rGO was negligible (inset of **Figure 5c**). The higher rates of formaldehyde generation by the 0.3 NiO/CeO_2 and $NiO/CeO_2/rGO$ photocatalysts can be associated to the roles played by NiO and rGO. NiO is widely used as a hole transfer agent, which can suppress charge carrier recombination. Owing to the formation of p-n junctions at $NiO-CeO_2$ interfaces, the number of electrons available for CO_2 reduction increased by the suppression of charge carrier

recombination. In addition, rGO works both as electron extractor and sequential electron shuttling agent, extracting electrons from CeO_2 and transferring to CO_2 molecules, as discussed earlier (in TRPL result section). In fact, multiple electrons can be sequentially transferred from CeO_2 surface to CO_2 molecules attached to its surface through the rGO layer, facilitating their reduction process. The whole process of light-induced oxygen vacancy formation at ceria surface, adsorption and activation of CO_2 molecules, multi-electron transfer and selective reduction of CO_2 molecule to produce formaldehyde has been schematically illustrated in **Figure 6**. The solar-to-fuel conversion efficiency ($\boldsymbol{\eta_{STF}}$) of the CO_2-to-formaldehyde reduction reaction stimulated by the NiO/CeO$_2$/rGO hybrid composite photocatalyst was calculated using equation (4):

$$\boldsymbol{\eta_{STF}}(\%) = \left[\frac{\text{Output energy of evolved formaldehyde}}{\text{Energy of incident solar light}} \right]_{\text{AM 1.5G}} \times 100$$

$$= \left[\frac{\Delta H_C°(\text{HCHO}) \times \text{mol (HCHO)}}{(1-T) \times P_{incident} \times \text{Area} \times \text{time}} \right]_{\text{AM 1.5G}} \times 100 \qquad (4)$$

where, $\Delta H_C°(HCHO)$ is the combustion energy of formaldehyde (561.1 kJ/mol),[50] T is the optical transmittance of the aliquot collected from the CO_2 reduction reactor, and $P_{incident}$ is the intensity of illumination. Optical transmittance of the NiO/CeO$_2$/rGO dispersed electrolyte was about 0.002, and the intensity of irradiation was one-sun solar light irradiation (100 mW/cm^2) over an illuminating area of 6.25 cm^2. The quantity of formaldehyde produced by the NiO/CeO$_2$/rGO hybrid composite photocatalyst for 1 h of solar light irradiation was 31.054 μmol for 0.05 g of catalyst, which is equivalent to 421.09 μmol of formaldehyde/g of photocatalyst/h. Substituting these values in equation (5), the $\boldsymbol{\eta_{STF}}$ value estimated for the reaction was 0.775%. As can be seen in **Table 2**, while most of the used ceria-based photocatalysts produced methanol

as unique liquid hydrocarbon fuel, our hybrid composite catalyst produced formaldehyde as single liquid fuel. On the other hand, the efficiency of CO_2 reduction and generation of formaldehyde by the hybrid composite catalyst is higher than the products reported for CeO_2-based composite photocatalysts [51-58] under similar experimental conditions. Moreover, the hybrid composite photocatalyst revealed its high photochemical stability (**Figure 5c**). After 5 cycles (5 h each) of reutilization, CO_2 reduction efficiency of the hybrid photocatalyst reduced only about 5%. As can be noticed from the data presented in **Table S2** (Supporting Information), while the incorporation of rGO enhances the specific surface area of the photocatalysts significantly, their CO_2 adsorption capacity remain almost unaffected. In fact, rGO-grafting blocks some of the active CO_2-capturing sites of CeO_2 (**Table S2**), reducing its CO_2 reduction capacity (**Figure 5c**). To verify that the obtained formaldehyde is the product of CO_2 reduction, not originated from any other source such as rGO, we performed the photocatalytic reactions over all the photocatalysts without CO_2 bubbling. However, formaldehyde production could not be detected in absence of CO_2 bubbling.

To study the mechanism of CO_2 reduction on the surface of NiO/CeO_2/rGO hybrid composite photocatalyst including its activation, *in-situ* ATR-IR spectra were recorded in a Nicolet iS50 spectrometer (from Thermo Fischer Scientific) utilizing a multi-bounce ZnSe horizontal attenuated total reflection (HATR) crystal, coated with a thin layer of NiO/CeO_2/rGO hybrid composite photocatalyst. As can be seen in **Figure 5d**, all the ATR-IR transmittance spectra (recorded at different reaction times) revealed a strong absorption signal around 2345 cm^{-1}, which is the signature absorption band of CO_2. A gradual increase in the intensity of this signal with reaction time indicates the consumption of CO_2 during reaction. Another absorption band with gradually increased intensity could be detected around 1060 cm^{-1}, which has been assigned

to carbonate species (CO_3^{2-}) in the literature.[59,60] Meanwhile, the appearance of absorption peak around 1393 cm^{-1} with decreasing intensity indicates the formation of another reaction intermediate. This peak was assigned to HCOO (formate).[61,62] The results obtained from *in-situ* ATR-IR analysis are consistent with the results obtained through *in-situ* XAFS analysis. During the photocatalytic process, CO_2 molecules dissolved in the reaction solution were adsorbed at the oxygen vacancy sites of CeO_2 and activated to unidentate CO_2. During the reduction of these activated CO_2 molecules, HCOO was formed as an intermediate. Based on the intermediates detected by *in-situ* XAFS and ATR-IR spectroscopies, a probable pathway for the complete reduction of CO_2 under solar light illumination has been presented in **Figure 6**. The initial step of this multi-step process is the light-induced vacancy formation at CeO_2 surface. In the second step, CO_2 molecules are adsorbed at oxygen vacancy sites of CeO_2 surface. The adsorbed CO_2 molecules have a resonance structure with a negative charge; i.e. as unidentate CO_2 species as detected through the 1060 cm^{-1} absorption band in ATR-IR spectra. In step 3, anionic oxygen incorporates at the oxygen vacancy site to compensate the vacancy. The vacancy filled by oxygen would have positive charge; however, the two neighboring Ce^{3+} ions will be oxidized to Ce^{4+} and donate two electrons; and the electrons in the C-O bond will be transferred to oxygen at vacancy site (step 4). According to Libuda's report, oxygen vacancies at the surface of CeO_2 can be oxidized spontaneously in presence of CO_2;[63] thus, the proposed mechanism is reasonable. Subsequently, a proton would be attached to the carbanion, resulting in the formation of formate (step 5), as detected by ATR-IR (peak at 1393 cm^{-1}). If one electron is supplied, the formate radical could be formed (step 6), and a proton would be attached to the anionic oxygen (step 7). The dissociation reaction occurs through the incorporation of one electron and one proton (steps 8 & 9), finally producing formaldehyde. Subsequently, stoichiometric CeO_2 can be

reduced by external light irradiation, regaining its catalytic activity. Therefore, the high CO_2 reduction ability of the fabricated $NiO/CeO_2/rGO$ hybrid composite nanostructures can be associated to the combined synergetic effects, i.e. light induced oxygen vacancy formation at CeO_2 surface, suppression of charge recombination at $NiO-CeO_2$ interface, and electron accumulation over rGO surface of the hybrid photocatalyst.

Although the formation of p-n junction at the $NiO-CeO_2$ interface is very clear from the Mott–Schottky plot of the sample presented in **Figure S8c** (Supporting Information), the increase in average carrier lifetime (τ_{ave}) due to integration of NiO with CeO_2 is not high ($\sim 5\%$ only), probably due to the small difference in band gap energy of the two materials (3.30 eV for CeO_2 and 3.41 eV for NiO). On the other hand, the change (reduction) in average lifetime due to rGO grafting is considerable ($> 60\%$); which indicates that the charge extraction and charge holding properties of rGO play major roles in the enhanced catalytic performance of the $NiO/CeO_2/rGO$ hybrid composite photocatalyst.

Conclusions

In summary, we demonstrate an efficient CO_2 reduction process by $NiO/CeO_2/rGO$ hybrid composite photocatalyst to produce formaldehyde selectively, under visible light illumination. The high CO_2 reduction ability (~ 4 times higher than the pristine CeO_2) of the photocatalyst to produce formaldehyde (421.09 $\mu mol\ g^{-1}\ h^{-1}$) can be associated to the formation of p-n junction at $NiO-CeO_2$ interface, along with the electron scavenging behavior of rGO sheets at the surface of the heterostructures. Formation of p-n junction at $NiO-CeO_2$ interface reduces the recombination rate of photogenerated charge carriers, enhancing their average lifetime. The photogenerated electrons are collected by rGO and transferred to the activated CO_2 molecules captured at oxygen

vacancy sites of CeO_2 surface. Formation of oxygen vacancies on CeO_2 surface due to solar light illumination could be monitored by *in-situ* XANEX spectroscopy. Structural changes occurred at the surface of CeO_2 due to the formation of oxygen vacancies could be monitored through *in-situ* XAFS analysis. Generation of $CO_2^{\bullet-}$ radical and formate as intermediate products of CO_2 reduction could be monitored by *in-situ* EPR and *in-situ* ATR-IR spectroscopy, respectively. Based on the obtained results, we presented a step-by-step description of the multi-step CO_2 reduction process, which can help the researchers not only to understand this complex process, but also for designing new, efficient catalysts for photocatalytic reduction of CO_2.

Acknowledgements

Author Contributions

Y. S. Kang supervised the research project and made conclusions, A. Pawar and U. Pal analyzed the results and prepared the manuscript. H. R. Park designed the concept, performed the experiments, and prepared the manuscript. T. Zhang analyzed the ATR-IR results and revision of the manuscript.

Conflicts of interest

There are no conflicts to declare.

Supporting Information

Supporting information is available in the online version of this article.

References

1. D. M. Etheridge, L. P. Steele, R. L. Langenfelds, R. J. Francey, J. M. Barnola, V. I. Morgan, J. Geophys. Res. 101 (1996) 4115-4128.

2. J. M. Matter, M. Stute, S. Ó. Snæbjörnsdottir, E. H. Oelkers, S. R. Gislason, E. S. Aradottir, B. Sigfusson, I. Gunnarsson, H. Sigurdardottir, E. Gunnlaugsson, et al. Science 352 (2016) 1312–1314.

3. Y. Qin, X. Wang, Biotechnol. J. 5 (2010) 1164–1180.

4. K. Hara, A. Kudo, T. Sakata, J. Electroanal. Chem. 421 (1997) 1–4.

5. M. N. Mahmood, D. Masheder, C. J. Harty, J. Appl. Electrochem. 17 (1987) 1223–1227.

6. F. Köleli, D. Balun, Appl. Catal. A 247 (2004) 237–242.

7. J. P. Jones, G. K. S. Prakash, G. A. Olah, Isr. J. Chem. 54 (2014) 1451–1466.

8. J. F. Debrito, A. R. Araujo, K. Rajeshwar, M. V. B. Zanoni, Chem. Eng. J. 264 (2015) 302−309.

9. C. W. Kim, M. J. Kang, S. Ji, Y. S. Kang, ACS Catalysis 8(2) (2018) 968-974.

10. A. U. Pawar, C. W. Kim, M. T. NguyenLe, Y. S. Kang, ACS Sustainable Chem. Eng. 7 (2019) 7431-7455.

11. J. Yu, J. Low, W. Xiao, P. Zhou, M. Jaroniec, J. Am. Chem. Soc. 136 (2014) 8839–8842.

12. H. Fujiwara, H. Hosokawa, K. Murakoshi, Y. Wada, S. Yanagida, T. Okada, H. Kobayashi, J. Phys. Chem. B 101 (1997) 8270–8278.

13. Y. Matsumoto, M. Obata, J. Hombo, J. Phys. Chem. 98 (1994) 2950–2951.

14. L. Wan, X. Wang, S. Yan, H. Yu, Z. Li, Z. Zou, CrystEngComm. 14 (2012) 154–159.

15. G. Sahara, O. Ishitani, Inorg. Chem. 54 (2015) 5096–5104.

16. A. J. Morris, R. T. McGibbon, A. B. Bocarsly, ChemSusChem. 4 (2011) 191–196.

17. D. Jiang, W. Wang, L. Zhang, Y. Zheng, Z. Wang, ACS Catal. 5 (2015) 4851–4858.

18. Z. Cheng, B. J. Sherman, C. S. Lo, J. Chem. Phys. 138 (2013) 014702 (1-12).

19. N. Kumari, M. A. Haider, M. Agarwal, N. Sinha, S. Basu, J. Phys. Chem. C 120 (2016) 16626–16635.

20. T. Staudt, Y. Lykhach, N. Tsud, T. Skála, K. C. Prince, V. Matolín, J. Libuda, J. Phys. Chem. C 115 (2011) 8716–8724.

21. M. Li, L. Zhang, M. Wu, Y. Du, X. Fan, M. Wang, L. Zhang, Q. Kong, J. Shi, Nano Energy 19 (2016) 145–155.

22. X. H. Lu, S. L. Xie, T. Zhai, Y. F. Zhao, P. Zhang, Y. L. Zhang, Y. X. Tong, RSC Advances 1 (2011) 1207–1210.

23. C. H. Zeng, S. Xie, M. Yu, Y. Yang, X. Lu, Y. Tong, J. Power Sources 247 (2014) 545–550.

24. H. Li, W. Zhang, W. Xu, T. Wang, G. Liu, X. Zhang, G. Qiao, Inorg. Chem. Commun. 83 (2017) 59–61.

25. Z. Zheng, N. Li, C. Q. Wang, D. Y. Li, Y. M. Zhu, G. Wu, Int. J. Hydrog. Energy 37 (2012) 13921–13932.

26. S. Xie, Z. Wang, F. Cheng, P. Zhang, W. Mai, Y. Tong, Nano Energy 34 (2017) 313–337.

27. J. Guo, K. Wang, X. Wang, Catal. Sci. Technol. 7 (2017) 6013–6025.

28. Z. Zhang, C. Shao, X. Li, C. Wang, M. Zhang, Y. Liu, ACS Appl. Mater. Interfaces 2(10) (2010) 2915–2923.

29. Z. Zhu, J. Ping, X. Huang, J. Hu, Q. Chen, X. Ji, C. E. Banks, J. Mater. Sci. 47 (2011) 503–507.

30. A. Renaud, B. Chavillon, L. Cario, L. L. Pleux, N. Szuwarski, Y. Pellegrin, E. Blart, E. Gautron, F. Odobel, S. Jobic, J. Phys. Chem. C 117 (2013) 22478–22483.

31. S. Hufner, Adv. Phys. 43 (1994) 183-156.

32. K. Das, S. K. De, J. Lumin. 129 (2009) 1015–1022.

33. T. Wang, Y. Wei, X. Chang, C. Li, A. Li, S. Liu, J. Zhang, J. Gong, Appl. Catal. B Environ. 226 (2018) 31–37.

34. T. Xie, Y. Liu, H. Wang, Z. Wu, Appl. Surf. Sci. 444 (2018) 320–329.

35. M. K. Kavitha, P. Gopinath, H. John, Phys. Chem. Chem. Phys. 17 (2015) 14647–14655.

36. R. Rameshbabu, R. Vinoth, M. Navaneethan, Y. Hayakawa, B. Neppolian, CrystEngComm 19 (2018) 2475–2486.

37. N. Zhu, K. Zheng, K. J. Karki, M. Abdellah, Q. Zhu, S. Carlson, D. Haase, K. Žídek, J. Ulstrup, S. E. Canton, T. Pullerits, Q. Chi, Sci Rep. 5 (2015) 9860 (1-14).

38. P. D. Tran, S. K. Batabyal, S. S. Pramana, J. Barber, L. H. Wong, S. C. J. Loo, Nanoscale 4 (2012) 3875–3878.

39. I. V. Lightcap, T. H. Kosel, P. V. Kamat, Nano Lett. 10 (2010) 577–583.

40. S. Mochizuki, F. Fujishiro, Phys. Status Solidi (b) 246(10) (2009) 2320–2328.

41. T. Ohashi, S. Yamazaki, T. Tokunaga, Y. Arita, T. Matsui, T. Harami, K. Kobayashi, Solid State Ion. 113-115 (1998) 559–564.

42. R. D. Shannon, Acta Cryst. A 32 (1976) 751–767.

43. J. D. Cafun, K. O. Kvashnina, E. Casals, V. F. Puntes, P. Glatzel, ACS Nano 7 (2013) 10726–10732.

44. E. Shoko, M. F. Smith, R. H. McKenzie, J. Phys.: Condens. Matter 22 (2010) 223201–19.

45. C. Song, Catal. Today 115 (2006) 2-32.

46. A. Gimat, V. Kasneryk, A. L. Dupont, S. Paris, F. Averseng, J. Fournier, P. Massiani, V. Rouchon, New J. Chem. 40 (2016) 9098-9110.

47. R. Zalma, L. Bonneau, J. Guignard, H. Pezerat, M. C. Jaurand, Toxicological and Environmental Chemistry, 13(3-4) (1987) 171-187.

48. J. E. Wertz, J. R. Bolton, Electron Spin Resonance, First Ed. New York: Chapman and Hall, 1972; 222.

49. X. Shi, N. Dalal, K. S. Kasprzak, Environmental Health Perspective Supplements, 102(1) (1994) 91-96.

50. G. Reuss, W. Disteldorf, A. O. Gamer, A. Hilt, Formaldehyde. Ullmann's encyclopedia of industrial chemistry. Weinheim: Wiley **2003**.

51. C. Yang, Q. Li, Y. Xia, K. Lv, M. Li, Appl Surf Sci. 464 (2019) 388–395.

52. M. Liang, T. Borjigin, Y. Zhang, B. Liu, H. Liu, H. Guo, Appl. Catal. B-Environ. 243 (2019) 566–575.

53. Y. Pu, Y. Luo, X. Wei, J. Sun, L. Li, W. Zou, L. Dong, Appl. Catal. B-Environ. 254 (2019) 580–586.

54. S. S. Zhou, S. Q. Liu, Photochem. Photobiol. Sci. 16 (2017) 1563.

55. J. Zhao, Y. Wang, Y. Li, X. Yue, C. Wang, Catal. Sci. Technol. 6 (2016) 7967.

56. M. Wang, M. Shen, X. Jin, J. Tian, M. Li, Y. Zhou, L. Zhang, Y. Li, J. Shi, ACS Catal. 9(5) (2019) 4573-4581.

57. H. Abdullah, M. R. Khan, M. Pudukudy, Z. Yaakob, N. A. Ismail, J. Rare. Earth 33(11) (2015) 1155.

58. Y. Wang, X. Bai, F. Wang, S. Kang, C. Yin, X. Li, J. Hazard. Mater. 372 (2019) 69–76.

59.   J. C. Lavalley, Catal. Today 27 (1996) 377–401.

60.   M. León, E. Díaz, S. Bennici, A.Vega, S. Ordóñez, A. Auroux, Ind. Eng. Chem. Res. 49 (2010) 3663–3671.

61.   M. N. Hossain, J. Wen, S. K. Konda, M. Govindhan, A. Chen, Electrochem. commun. 82 (2017) 16–20.

62. D. B. Clarke, D. K. Lee, M. J. Sandoval, A. T. Bell, J. Catal. 150 (1994) 81–93.

63.   T. Staudt, Y. Lykhach, N. Tsud, T. Skála, K. C. Prince, V. Matolín, J. Libuda, J. Catal. 275 (2010) 181–185.

List of Tables and Figures

Table 1. Kinetic parameters for TRPL fitting curves of CeO_2, 0.3 NiO/CeO_2 and $NiO/CeO_2/rGO$ photocatalysts

	A_1	τ_1 (ns)	A_2	τ_2 (ns)	τ_{ave} (ns)
CeO_2	0.4912	8.11	1.379	1.84	5.67
0.3 NiO/CeO_2	0.8700	8.20	2.520	1.71	5.80
$NiO/CeO_2/rGO$	0.1429	4.00	1.650	0.3435	2.16

Table 2. Ceria-based hybrid composite photocatalysts and their CO_2 reduction performance.

| Photocatalyst	Light source	Products	Yield	References
$CeO_2/ZnIn_2S_4$	300 W Xenon lamp	Methanol (CH_3OH)	0.542 ($\mu mol\ g^{-1}\ h^{-1}$)	[51]
$g\text{-}C_3N_4@CeO_2$	300 W Xenon lamp	Methane (CH_4), CH_3OH, Carbon monoxide (CO)	CH_4 (3.5 $\mu mol\ g^{-1}$), CH_3OH (5.2 $\mu mol\ g^{-1}$), CO (16.8 $\mu mol\ g^{-1}$)	[52]
Cu_2O/CeO_2	300 W Xenon lamp	CO	~0.140 ($\mu mol\ g^{-1}\ h^{-1}$)	[53]
Cu(II)/ING/CeO$_2$ (CeO_2 loaded N-doped graphene and Cu(II))	250 W Xenon lamp	CH_3OH	385.8 ($\mu mol\ g^{-1}\ h^{-1}$)	[54]
CeO_2/TiO_2	500 W Xenon lamp	CO, CH_4	CO (~10 $\mu mol\ g^{-1}h^{-1}$), CH_4 (~4 $\mu mol\ g^{-1}h^{-1}$)	[55]
$Cu/CeO_{2\text{-}x}$	300 W Xenon lamp	CO	1.65 ($\mu mol\ g^{-1}h^{-1}$)	[56]
$CeO_2\text{-}TiO_2$	500 W Xenon lamp	CH_3OH	~3.1 ($\mu mol\ g^{-1}h^{-1}$)	[57]
Cr doped CeO_2	500 W Xenon lamp	CO	~2.1 ($\mu mol\ g^{-1}h^{-1}$)	[58]
$NiO/CeO_2/rGO$	300 W Xenon lamp	Formaldehyde (HCHO)	421.09 ($\mu mol\ g^{-1}\ h^{-1}$)	*Present Work*
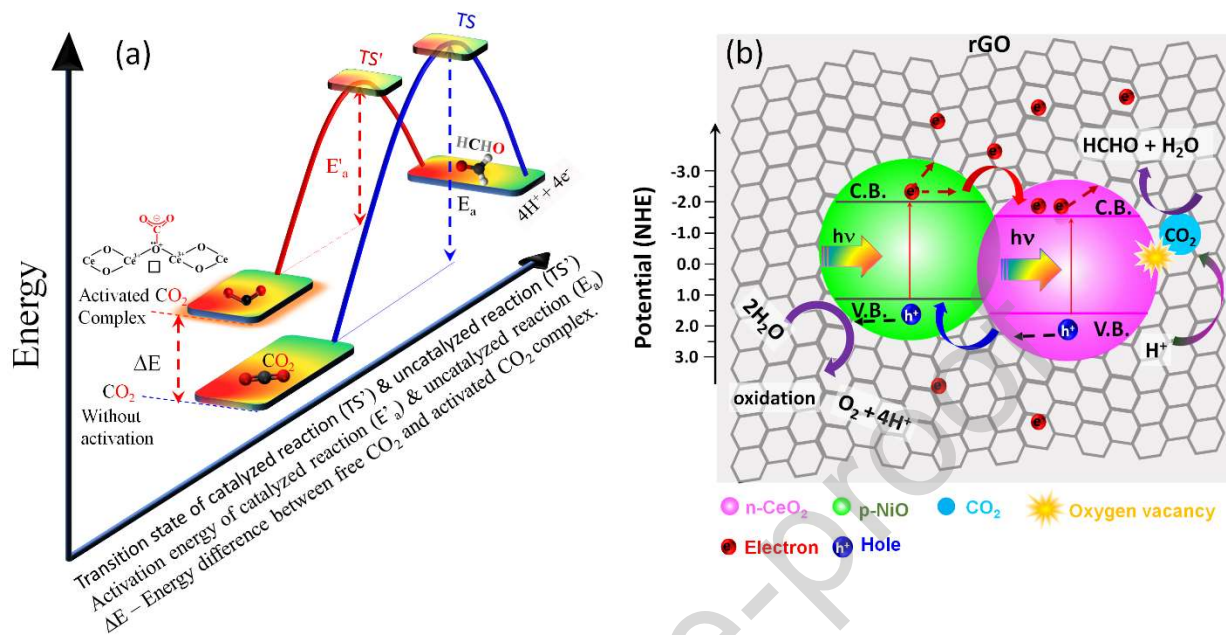
Figure 1. Schematic presentation of (a) change in energy level of free CO_2 and activated CO_2 by CeO_2 and (b) photocatalytic CO_2 reduction process on $NiO/CeO_2/rGO$ hybrid composite photocatalyst.
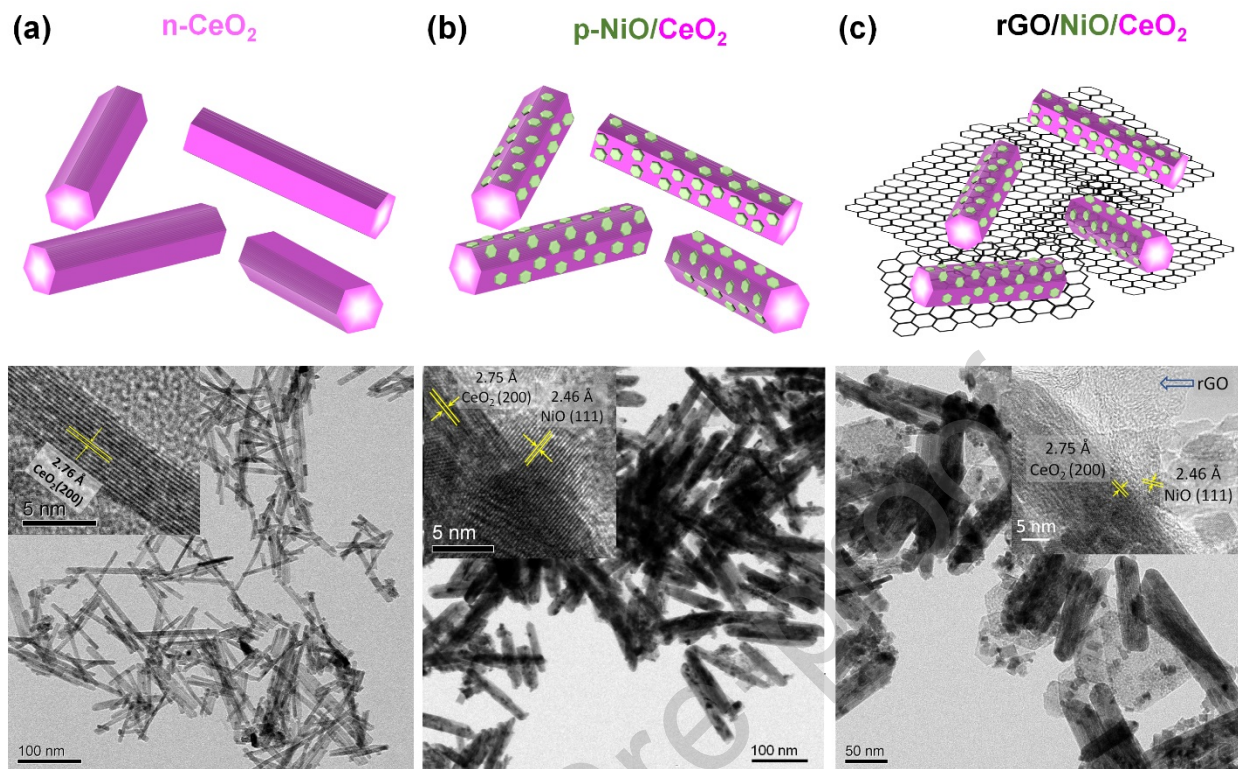
Figure 2. Typical TEM images of the synthesized (a) n-CeO$_2$ nanorods, (b) p-NiO/CeO$_2$ composite, and (c) NiO/CeO$_2$/rGO hybrid composite with their schematics (upper case). Insets of (a) and (b) are the typical HRTEM images of corresponding nanostructures.
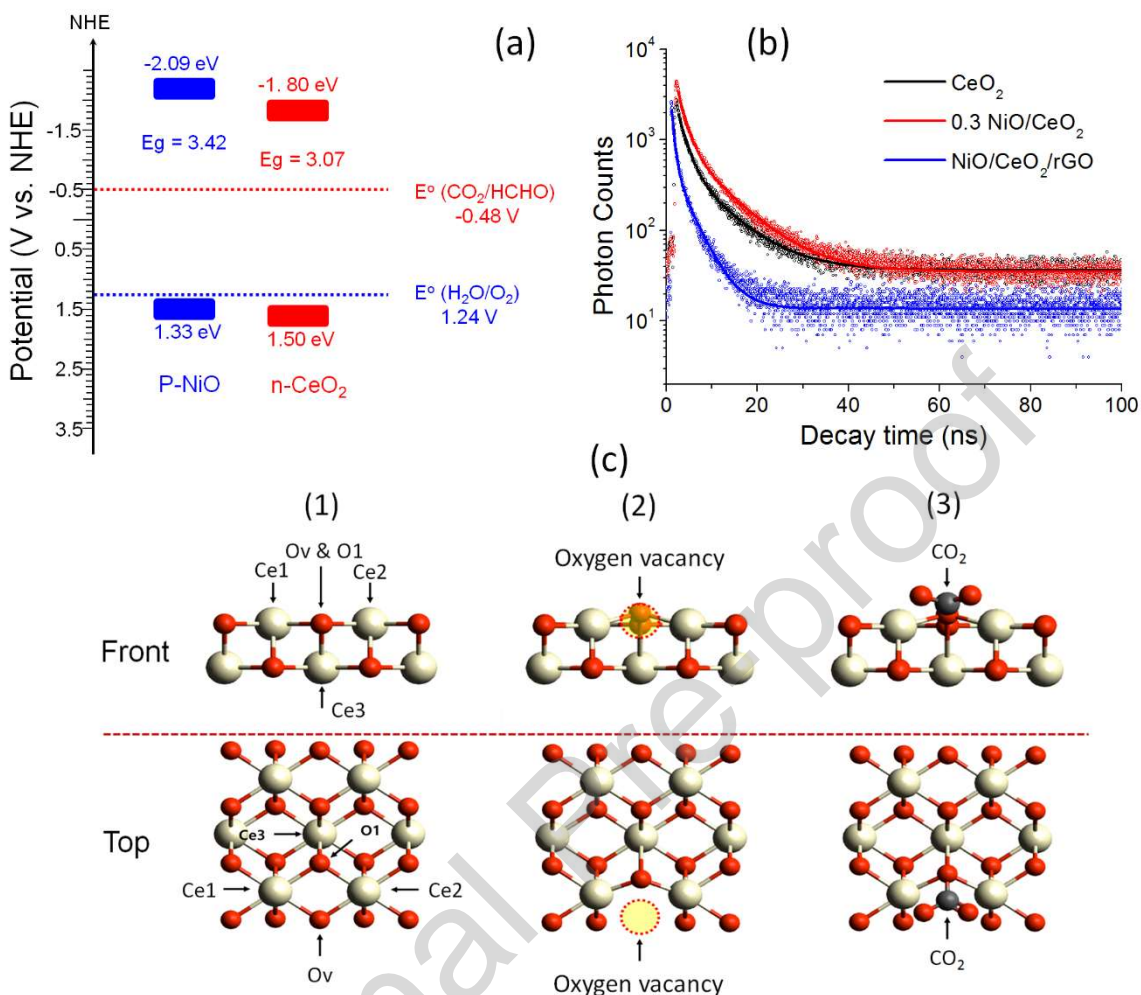
Figure 3. (a) Energy band alignment of p-NiO (blue) and n-CeO$_2$ (red) in the NiO/CeO$_2$/rGO hybrid composite photocatalyst. (b) Time-resolved PL decay curves of CeO$_2$ (black), 0.3 NiO/CeO$_2$ (red) and NiO/CeO$_2$/rGO (blue) hybrid composite photocatalyst. Continuous lines are the double-exponential fitted curves. As can be seen in Table 1, τ_1 and τ_2, and hence the τ_{ave} values for the three catalysts are different. The offset between the background decay vanishes after a couple of minutes of the cessation of excitation. (c) Structure of (1) stochiometric CeO$_2$, (2) oxygen vacancy generated CeO$_{2-\delta}$, and (3) CO$_2$ molecule captured at oxygen vacancy site of CeO$_2$. Upper case structures are the front views and lower case structures are the top views.
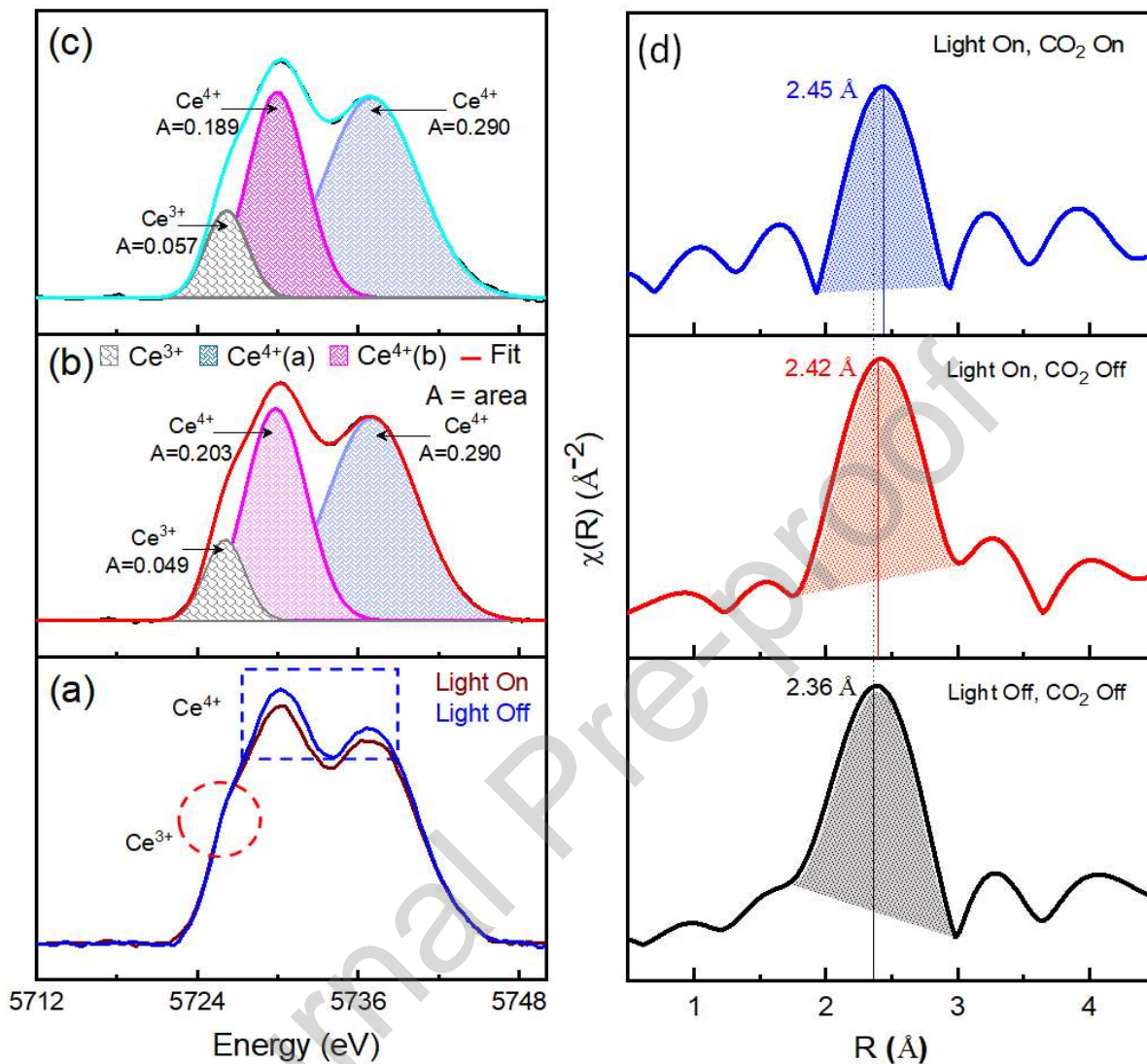
Figure 4. *In-situ* XANES plots of NiO/CeO$_2$/rGO photocatalyst (a) without and with solar light irradiation. Deconvoluted XANES plot of (b) without solar light irradiation, and (c) with solar light irradiation. (d) *In-situ* EXAFS plots of NiO/CeO$_2$/rGO photocatalyst in different conditions. The black trace corresponds to light off condition without CO$_2$ bubbling, the red trace corresponds to light on condition without CO$_2$ bubbling, and the blue trace corresponds to light on condition with CO$_2$ bubbling. Phase corrected R(Ce-O) of light off and no CO$_2$ bubbling condition was 2.36 Å, light on without CO$_2$ bubling condition was 2.42 Å, and light on with CO$_2$ bubling condition was 2.45 Å.
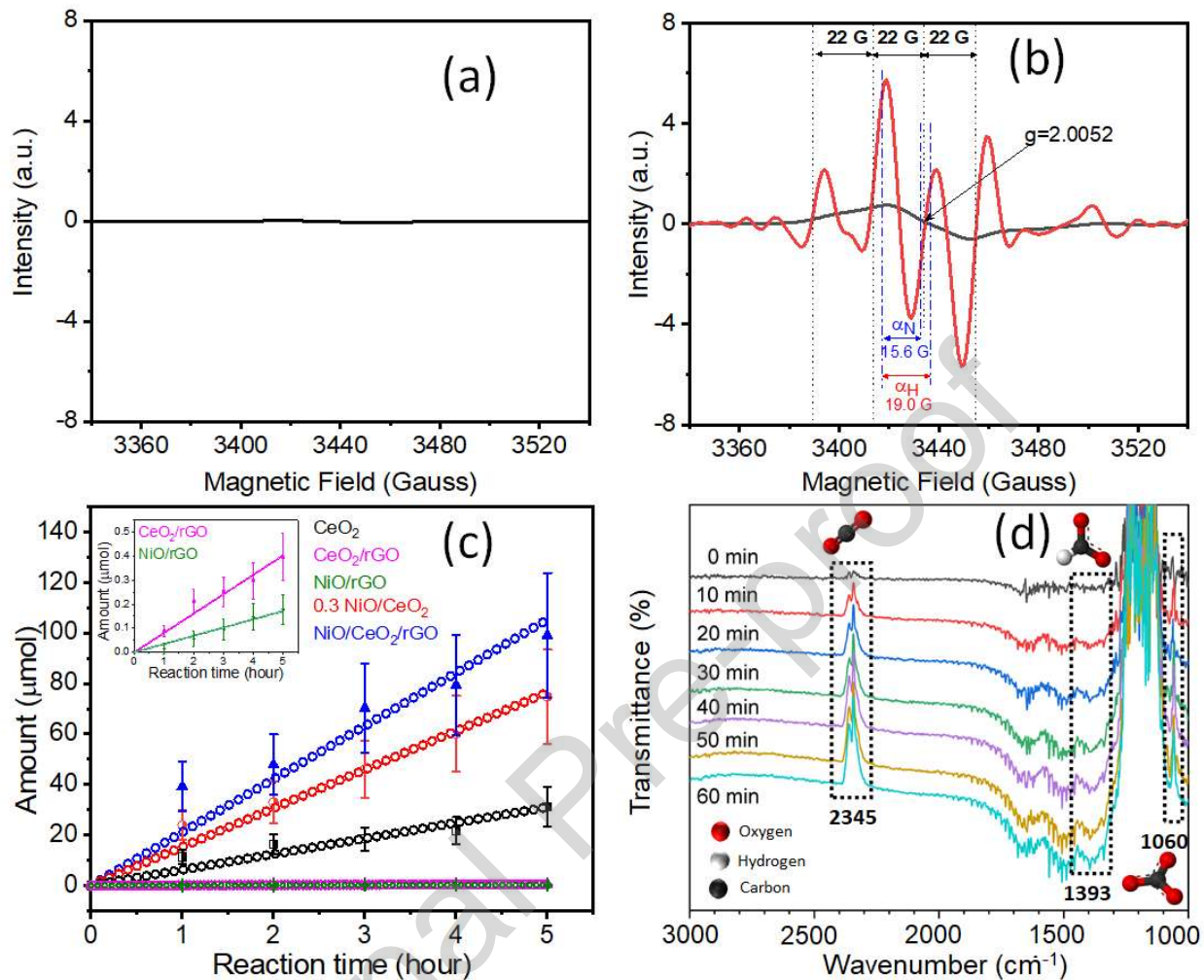
Figure 5. *In-situ* EPR spectra of synthesized CeO_2 in 0.1 M DMPO solution before (a) and after (b) CO_2 reduction reaction, red color shows deconvoluted EPR spectrum. (c) GC estimated quantity of formaldehyde produced during CO_2 reduction reaction over CeO_2 (black), 0.3 NiO/CeO_2 (red), 0.3 NiO/rGO (green), CeO_2/rGO (magenta) and $rGO/NiO/CeO_2$ (blue) photocatalysts in 50 mL of 0.2 M $NaHCO_3$ & 0.2 M Na_2SO_3 mixture solution; 0.05 g of each of the catalysts was used for photocatalytic CO_2 reduction. Data point error bars in (c) correspond to the variation in production yield during 6 cycles (5 h each) of reutilization of the photocatalysts. The catalysts NiO/rGO and CeO_2/rGO produce very little amount of formaldehyde. The CO_2 reduction yields of the two catalysts have been presented in amplified scale as inset of (c). (d) *In-situ* ATR-IR spectra recorded during CO_2 reduction reaction on $NiO/CeO_2/rGO$ hybrid composite photocatalyst.

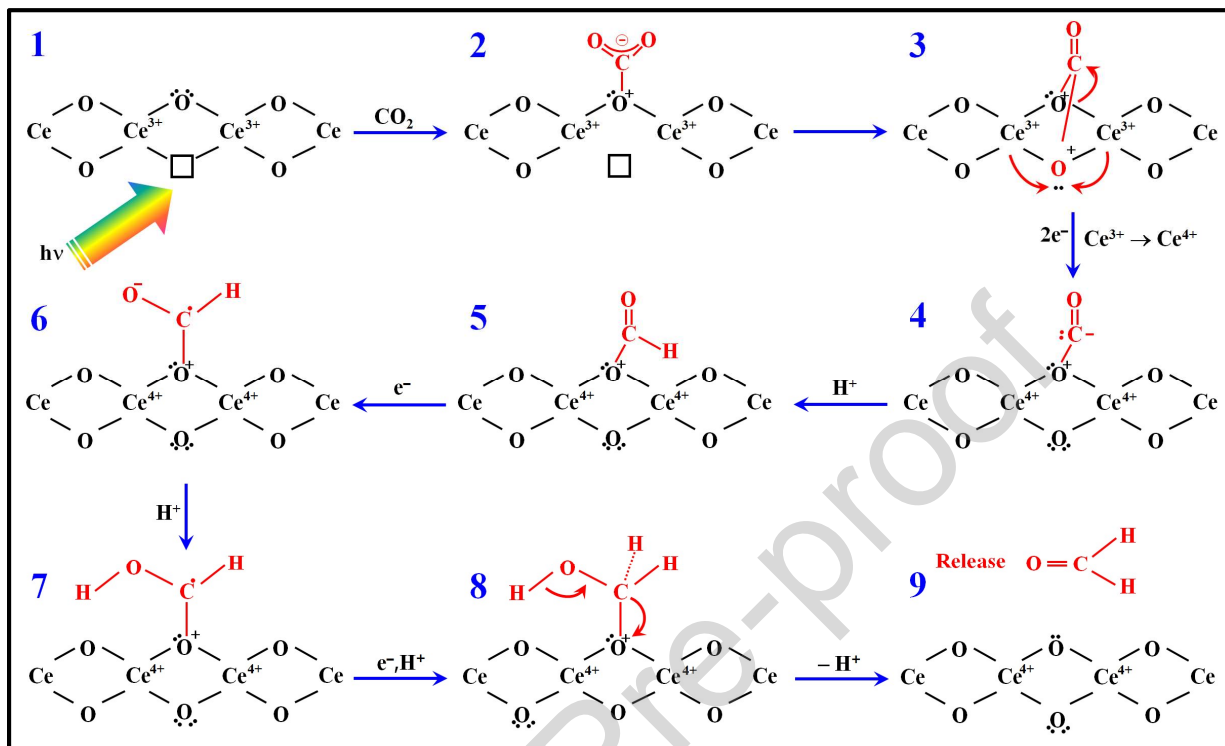**Figure 6.** Reaction mechanism and pathways associated to photoactivation of CO_2 molecules at oxygen vacancy sites of CeO_2 surface and CO_2 reduction through proton-coupled electron transfer processes at different stages of reaction. Blank squares correspond to photo-induced oxygen vacancies generated in step 1. CO_2 capture occurs at the oxygen site adjacent to oxygen vacancy in step 2. In step 3, adsorbed CO_2 molecules get activated by sharing O with vacancy site. Electron sharing between Ce and O atoms at vacancy site occurs in step 4. In step 5, transformation of activated CO_2 molecule to formate by capturing a proton occurs. In step 6, formation of formate radical occurs through electron transfer from rGO. Attachment of a proton (generated from water oxidation) to the oxygen of formate radical happens in step 7. Finally, formaldehyde is produced through electron and proton transfer processes in steps 8 & 9.

Credit Author Statement

H. R. Park designed the concept, performed the experiment, and prepared the manuscript

A. U. Pawar performed the experiment, analyzed the results, and prepared the manuscript

U. Pal analyzed the results and prepared the manuscript.

T. Zhang analyzed the ATR-IR results and revision of the manuscript.

Y. S. Kang supervised the research project and made conclusions.

Declaration of interests

☒ The authors declare that they have no known competing financial interests or personal relationships that could have appeared to influence the work reported in this paper.

☐The authors declare the following financial interests/personal relationships which may be considered as potential competing interests:

Highlights

➢ A rGO-grafted NiO-CeO$_2$ heterojunction nanocomposite was fabricated through a simple hydrothermal process to utilize in ptotocatalytic reduction of CO$_2$.

➢ The hybrid nanocomposite reduces CO$_2$ to formaldehyde liquid fuel under solar light irradiation.

➢ The hybrid nanocomposite produces formaldehyde at four times higher rate (421.09 mmolg^{-1}h^{-1}) than pristine CeO$_2$ nanostructures.

➢ Formation of photoinduced oxygen vacancy at CeO$_2$ surface and CO$_2^{\bullet-}$ radicals during photocatalytic reduction were monitored by *in-situ* XANEX and *in-situ* EPR spectroscopy.

➢ A step-by-step description of the multi-step CO$_2$ photoreduction process has been provided.